ACS Sustainable Chemistry & Engineering

Research Article

Cite This: ACS Sustainable Chem. Eng. 2019, 7, 5393−5403

pubs.acs.org/journal/ascecg

Rational Synthesis of Novel Phosphorylated Chitosan-Carboxymethyl Cellulose Composite for Highly Effective Decontamination of U(VI)

Yawen Cai,[†,‡,#] Lei Chen,[‡,#] Shitong Yang,[*,§] Lin Xu,[‡] Haibo Qin,[∥] Zhiyong Liu,[‡] Lanhua Chen,[‡] Xiangke Wang,[†,‡] and Shuao Wang[*,‡]

[†]College of Environment and Chemical Engineering, North China Electric Power University, No. 2 Beinong Road, Beijing 102206, People's Republic of China

[‡]State Key Laboratory of Radiation Medicine and Protection, School for Radiological and interdisciplinary Sciences (RAD-X) and Collaborative Innovation Center of Radiation Medicine of Jiangsu Higher Education Institutions, Soochow University, No. 199 Renai Road, Suzhou 215123, People's Republic of China

[§]Department of Earth and Planetary Science, Graduate School of Science, The University of Tokyo, 7-3-1 Hongo, Bunkyo-ku, Tokyo 113-0033, Japan

[∥]State Key Laboratory of Environmental Geochemistry, Institute of Geochemistry, Chinese Academy of Sciences, No. 99 Lincheng West Road, Guiyang 550081, People's Republic of China

ABSTRACT: In the present study, the phosphorylated chitosan (CSP) and phosphate-decorated carboxymethyl cellulose (CMCP) were cross-linked to synthesize a water-stable CSP-CMCP composite. Fourier transform infrared spectroscopy (FTIR) analyses indicated the occurrence of a dehydration-condensation reaction between amino and carboxyl groups as well as the introduction of abundant phosphate sites on CSP-CMCP surfaces. The maximum adsorption capacity of CSP-CMCP toward U(VI) (i.e., 977.54 mg/g at pH = 5.0 and T = 293 K) was superior to a series of adsorbents reported in the previous studies. In addition, CSP-CMCP showed an extremely high affinity for the selective capture of U(VI) from a simulated wastewater with multiple competing metal ions. The integrated analyses of X-ray diffraction, FTIR, X-ray photoelectron spectroscopy, X-ray absorption near edge structure, and extended X-ray absorption fine structure spectroscopy suggested that the predominant U(VI) species formed inner-sphere surface complexes with the active phosphate groups, while a small proportion of U(VI) was reduced to a lower U(IV) state by the amino sites. These research findings highlighted the potential applicability of the CSP-CMCP composite for the remediation of uranium-bearing wastewater.

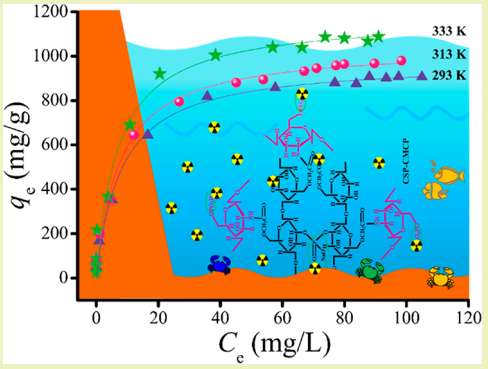

KEYWORDS: *CSP-CMCP composite, U(VI), Removal performance, Selective capture, Spectroscopic analyses*

INTRODUCTION

The anthropogenic nuclear activities discharge a series of toxic radionuclides (e.g., ^{60}Co, ^{90}Sr, ^{99}Tc, ^{131}I, $^{152+154}$Eu, $^{235+238}$U, ^{237}Np, ^{239}Pu, ^{241}Am, and ^{244}Cm) into the soil and water systems. Uranium, as the core element in nuclear industries and the component in nuclear waste, is harmful to the organisms due to its radiochemical and toxicological effects. The excess inhalation, ingestion, or percutaneous absorption of radioactive uranium will disturb the basic functions of lung, kidney, brain, and reproductive system in humans.[1] Hence, it is imperative to design advanced technologies and versatile materials for the highly efficient removal of uranium from the polluted water bodies.

Adsorption is one of the most popular techniques for capturing heavy metal pollutants owing to its superiorities of cost effectiveness, handy operation, high practicability and extensively optional adsorbents.[2,3] So far, a series of inorganic minerals with abundant resources, metal organic frameworks (MOFs) with porous feature and carbon-based nanocomposite with high surface area have been synthesized for the decontamination of U(VI).[4−8] However, these materials are not satisfactory enough in both the adsorption capability and selectivity toward U(VI). Besides, the complicated synthesis process, high cost and potential ecotoxicity of MOFs and nanocomposite further limit their application in the real wastewater disposal. Carbohydrate polymers (e.g., chitosan (CS), carboxymethyl cellulose (CMC), agarose, and alginate) and their functionalized derivatives are known as good chelating agents for heavy metal ions and radionuclides.[9,10] Unfortunately, these adsorbents exist as a disadvantage of poor physicochemical stability in aqueous solution. Based on the

Received: December 7, 2018
Revised: January 18, 2019
Published: January 29, 2019

DOI: 10.1021/acssuschemeng.8b06416
ACS Sustainable Chem. Eng. 2019, 7, 5393−5403

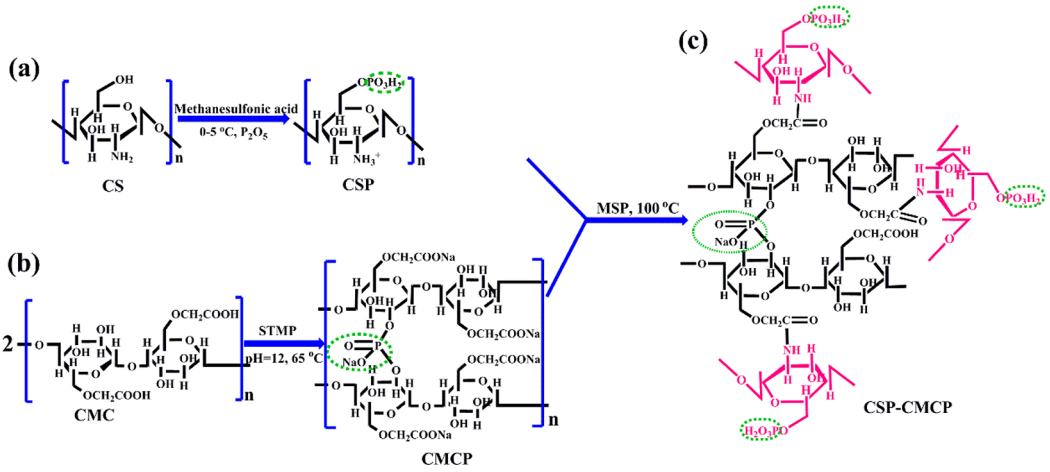

Figure 1. Schematic diagrams for the synthetic procedures and molecular structures of (a) CSP, (b) CMCP, and (c) CSP-CMCP.

above observations, it is imperative to design novel adsorbents with the combined merits of good chemical stability, environmental friendliness, excellent adsorption performance, and favorable affinity toward U(VI).

In this work, CS and CMC were chosen as the precursors due to their abundant sources, low cost, nontoxic, favorable biocompatibility, strong metal-chelating capacity, and easy functionalization.[11,12] In general, the coordination chemistry of actinides is dominated by its "hardness" and f-electrons. As a "hard" Lewis acid, U(VI) tends to form stable complexes with the "hard" Lewis bases, for example, the ligands that contain oxygen and nitrogen donors such as carboxyl, phosphate, phosphonate, amino, amidoxime, and so on.[13−15] According to this theoretical foundation, the P-bearing adsorbents are expected to display excellent adsorption affinity toward U(VI). In this work, the CS and CMC precursors were first modified by two different phosphorus-containing ligands. A subsequent cross-linking between the phosphorylated CS and the phosphate-decorated CMC was conducted to generate a novel and stable CSP-CMCP composite. The removal performance and relative affinity of this material for U(VI) was carefully studied under the effect of multiple environmental parameters including solution pH, ionic strength, temperature and coexisting heavy metal ions. Additional spectroscopic technologies, including XRD, FTIR, XPS, XANES, and EXAFS, were employed to clarify the underlying retention mechanisms of U(VI) by CSP-CMCP.

EXPERIMENTAL SECTION

Materials and Reagents. CS (Degree of deacetylation >95%, 100−200 mpa·s), CMC (MW = 700000, DS = 0.9, 2500−4500 mpa·s) and trisodium trimetaphosphate (STMP) were obtained from the Shanghai Yuanye Bio-Technology Co. Ltd. Methanesulfonic acid, monosodium phosphate (MSP), and phosphorus pentoxide (P_2O_5) were bought from J&K Scientific Ltd.. $UO_2(NO_3)_2{\cdot}6H_2O$ was received from commercial supplier. All other reagents with the analytical purity grade were directly used in the experiments without further treatment. A certain quality of $UO_2(NO_3)_2{\cdot}6H_2O$ was dissolved in Milli-Q water to prepare the stock solution of U(VI).

Preparation of CSP, CMCP, and CSP-CMCP. The phosphorylation of CS was carried out in a methanesulfonic acid-phosphorus pentoxide system.[16] This approach had multiple advantages such as mild synthesis condition, high modification efficiency, and ease of operation.[17] In brief, 2 g of CS was dissolved into 14 mL of methanesulfonic acid to prepare a viscous solution, and then 2 g of P_2O_5 was slowly added with homogeneous mixing. The mixture was moved into an ice bath and manually stirred with a glass rod for 2−3 h. During the reaction, the mouth of the flask was sealed with plastic wrap so as to prevent the adsorption of water molecules. Excessive ether was used to precipitate the resulting phosphorylated product (i.e., CSP). The obtained colloid was successively washed by using ether (×3), acetone (×3), and methanol (×3) and then dissolved into Milli-Q water before it was lyophilized. According to the previous study,[16] the obtained CSP was a water-soluble composite with a relatively high degree of substitution (DS). Meanwhile, the CS molecules retained the amino groups after phosphorylation, which would be beneficial for its further modification.

STMP was used as the phosphating agent for synthesizing the phosphorylated CMC (i.e., CMCP). The phosphorylation was based on the cross-linking between the ring-opened STMP and the hydroxyl (−OH) groups of CMC in diluted NaOH solution (1%). Under alkaline conditions, the negatively charged carboxyl ($-COO^-$) sites in the CMC molecules can provoke strong electrostatic repulsion among the polysaccharide chains. This situation will correspondingly facilitate the interaction of STMP with the −OH sites of the CMC polysaccharide units.[18] Briefly, a 200 mL solution containing 2 g of CMC was prepared by using the alkaline water (pH = 12 adjusted by 2.0 mol/L of NaOH). A total of 50 mL of 30% (w/v) STMP was added into the solution to activate the hydroxyl groups in the disaccharide units. The mixture (with the pH value maintained at ∼12.0) was gently stirred at 25 °C for 2 h followed by a vigorous stirring at 65 °C for 5 h. The product was dried at 45 °C until a translucent, flowing membranous material was obtained. The membrane was soaked in a large amount of Milli-Q water (×3) and then lyophilized. Herein, the as-prepared CSP and CMCP were water-soluble and could not be directly used in capturing uranium from solution. Therefore, CSP and CMCP were further cross-linked via a dehydration condensation process to obtain a water-stable CSP-CMCP composite.[19] In specific, 0.5 g of CSP and 0.5 g of CMCP were dissolved into 10 mL of Milli-Q water, respectively. These two suspensions were mixed with 2 g MSP and vigorously stirred at 100 °C for a time period of 1 h. The hot solution was then dumped into a 6 cm glass culture dish and the reactant was transferred into a muffle furnace that was preheated to 100 °C. After 6 h, the solution was dried by evaporation and a yellow pie-like dense polymer film was obtained. The film was washed by 100 mL of dilute HCl (0.01 mol/L), 100 mL of H_2O, 100 mL of dilute NaOH (0.01 mol/L), 100 mL of H_2O, and 50 mL of methanol in sequence to remove the unreacted substance and impurities. The purified CSP-CMCP film was vacuum-dried at 55 °C, grinded by an agate mortar, and then screened by using a 200-mesh sieve to get a fine powder. The chemical structures of the synthesized CSP, CMCP, and CSP-CMCP are displayed in Figure 1.

Characterizations. The FTIR spectra of the raw materials (i.e., CS, CMC) and the prepared composite (i.e., CSP, CMCP, and CSP-

DOI: 10.1021/acssuschemeng.8b06416
ACS Sustainable Chem. Eng. 2019, 7, 5393−5403

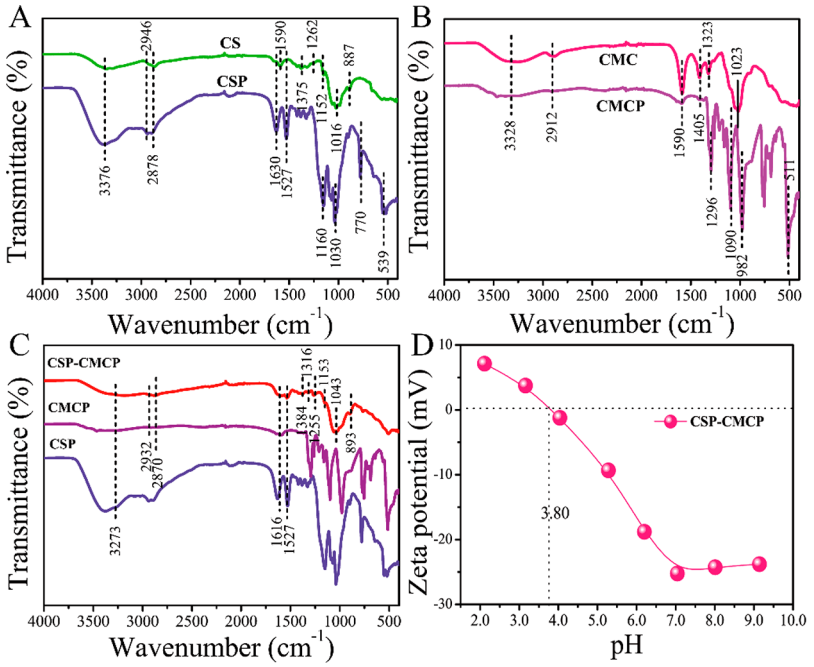

Figure 2. FTIR spectra of CS and CSP (A), CMC and CMCP (B), CSP, CMCP, and CSP-CMCP(C); (D) Zeta potentials of CSP-CMCP as a function of solution pH, T = 293 K, m/V = 0.05 g/L, I = 0.01 mol/L $NaNO_3$.

CMCP) were recorded with a Nicolet 6700 spectrometer (Thermo Scientific). The zeta potentials of CSP-CMCP composite within the pH range of 2.0−10.0 were measured by using a Zetasizer Nano ZS90 Analyzer. The TEM image and elemental maps of CSP-CMCP after U(VI) adsorption were collected on FEI Tecnai G2 spirit BioTwin Transmission Electron Microscope with the operating voltage of 120 kV. The physicochemical stability of CSP-CMCP in solution was carefully evaluated under a series of solution pH values. Specifically, the stock solution of CSP-CMCP composite was mixed with a series of sodium nitrate ($NaNO_3$) solutions to obtain an adsorbent content of 0.05 g/L. Herein, the usage of $NaNO_3$ as the background electrolyte was based on the wide existence of sodium (Na^+) and nitrate (NO_3^-) in the natural water systems and the industrial effluents. The pH values were carefully adjusted with negligible volumes of HNO_3/NaOH solutions with different concentration gradients. Note that the increase of total volumes for the reaction systems due to pH adjustments is negligible (several to dozens of μL). Accordingly, the deviation of the CSP-CMCP dosage is lower than 1%. Then, the suspensions were shaken for about 24 h, and the solid and liquid phases were separated by centrifuging at 8000g for 10 min. The supernatants were seriatim passed through 0.22 μm filters and the amounts of released phosphorus (P) were quantified by an inductively coupled plasma-atomic emission spectrometer (ICP-AES, Thermo Scientific iCAP 7000 series).

Batch Experiments. The removal performance of CSP-CMCP composite toward U(VI) was explored by conducting a series of batch experiments. In brief, the stock solutions of CSP-CMCP, $NaNO_3$, and U(VI) were mixed, pH adjusted, oscillated, centrifuged, and filtered by adopting the experimental procedures as mentioned above. The concentrations of U remaining in the solution were initially determined using ICP-AES with a detection limit of 0.08 ppm. Then, the samples with U concentrations lower than 0.08 ppm were further diluted and submitted for inductively coupled plasma-mass spectrometer (ICP-MS, Thermo Scientific ELEMENT 2/HR) measurement. The detection limit of U by using ICP-MS was 0.1 ppb. The adsorption percentage ($S\% = (C_0 - C_e)/C_0 \cdot 100\%$) and amount ($q_e = (C_0 - C_e) \cdot V/m$, mg/g) were calculated from the initial concentration of U(VI) (C_0, mg/L), the residual concentration of U(VI) (C_e, mg/L), and the dosage of CSP-CMCP (m/V, g/L). All the adsorption experiments were performed in triplicate, and each data point was measured for three times to obtain repeatable and accurate values. The standard deviation of the data was less than 5%.

To further explore the adsorption selectivity of CSP-CMCP toward U(VI), additional competitive adsorption experiments were conducted in a mixed solution containing multiple metal ions, that is, divalent strontium(II), cobalt(II), cadmium(II), and copper(II), trivalent chromium(III), lanthanum(III), europium(III), and ytterbium(III), as well as hexavalent uranium(VI). A parameter named selectivity coefficient (S_U, eq 1) was adopted to describe the relative adsorption affinity of CSP-CMCP toward U(VI):[20]

$$S_U = \frac{q_{e,U}}{q_{e,total}} \times 100\% \quad (1)$$

In the above equation, $q_{e,U}$ (mg/g) represents the U(VI) adsorption amount in the multicomponent system and $q_{e,total}$ (mg/g) represents the total adsorbed amount of all the metal ions by per weight CSP-CMCP composite.

Spectroscopic Analyses. By refereeing to the batch experiments, as described above, the U(VI)-containing sample for XRD, FTIR, XPS, and XAS analyses was prepared in a 250 mL triangular flask. Typically, the U(VI)-loaded wet pastes were moved into a sealed Ziploc bag and settled in cold storage. XRD patterns were analyzed by using a Bruker D8 Advance diffractometer with a Cu Kα radiation. XPS data were collected on an Axis UltraDLD X-ray photoelectron spectrometer (Kratos Analytical) equipped with a monochromatic Al Kα source. XANES and EXAFS spectra of U L_{III} edge were acquired at the BL14W1 beamline of Shanghai Synchrotron Radiation Facility (China) in the transmission mode. The obtained spectra were processed by using Athena and Artemis software.[21] Based on the crystallographic information files of $UO_2(CH_3COO)_2 \cdot 2H_2O$, $UO_2(NH_2)_2O(H_2O)_3$, $CaU(PO_4)_2 \cdot H_2O$, and $HUO_2PO_4 \cdot 4H_2O$, the theoretical phase shift functions and amplitudes of U−O, U−C/N, U−P, and U−U paths were calculated by FEFF 7.0.[5,22−24]

RESULTS AND DISCUSSION

Characterization. The FTIR data of CS, CSP, CMC, CMCP, and CSP-CMCP are shown in Figure 2A−C. For pristine CS (Figure 2A), the broad band at 3376 cm^{-1} results from the combined stretching vibration signals of −OH and

DOI: 10.1021/acssuschemeng.8b06416
ACS Sustainable Chem. Eng. 2019, 7, 5393−5403

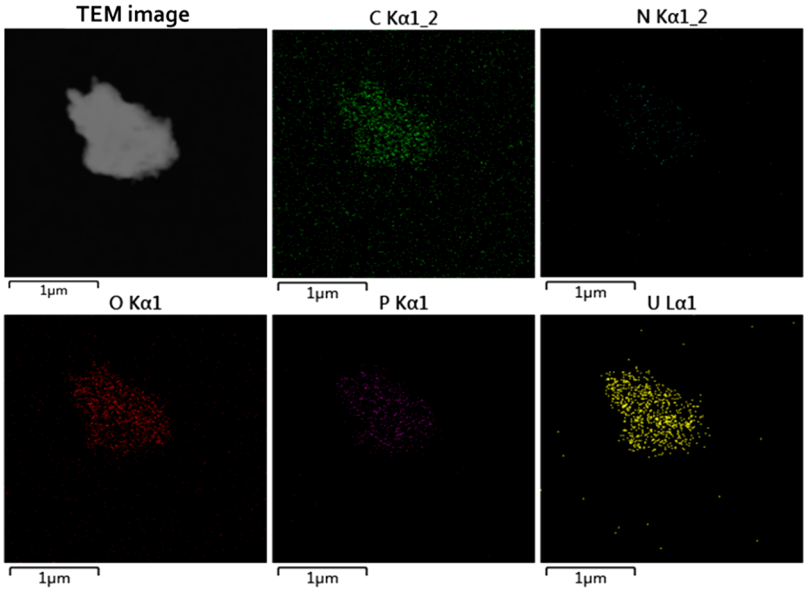

Figure 3. TEM image and elemental mapping of U(VI)-adsorbed CSP-CMCP composite.

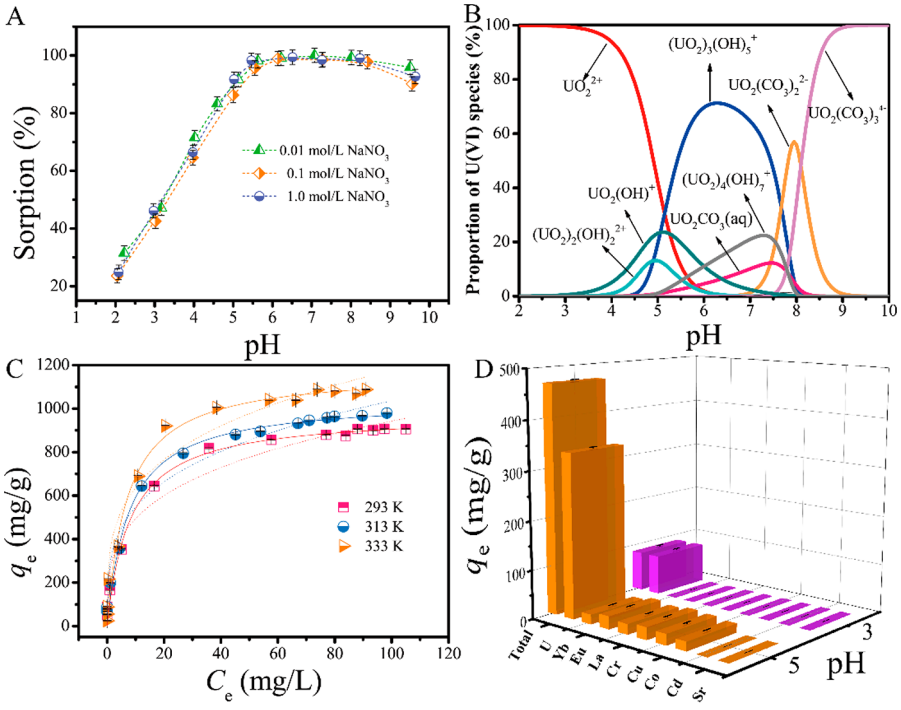

Figure 4. (A) Adsorption trends of U(VI) on CSP-CMCP as a function of pH and ionic strength. T = 293 K, m/V = 0.05 g/L, $C_{U(VI)initial}$ = 5.0 × 10^{-5} mol/L; (B) pH-dependent speciation of U(VI) in solution. T = 293 K, $C_{U(VI)initial}$ = 5.0 × 10^{-5} mol/L, I = 0.01 mol/L $NaNO_3$; (C) Adsorption isotherms, Langmuir and Freundlich model fits of U(VI) on CSP-CMCP. pH = 5.0, m/V = 0.05 g/L, I = 0.01 mol/L $NaNO_3$. Symbols represent the experimental data, solid lines represent Langmuir model fits and dash lines represent Freundlich model fits; (D) Adsorption selectivity of CSP-CMCP toward multiple metal ions. T = 293 K, pH = 3.0 and 5.0, m/V = 0.05 g/L, $C_{single\ metal\ ion}$ = 5.0 × 10^{-4} mol/L.

$-NH_2$ groups. The enhancement of this peak intensity after phosphorylation is due to the improved hydrophilic CSP. The FTIR spectrum of CSP exhibits characteristic P−O stretching vibrations (i.e., ν1 [PO_4] mode) at 1160 and 1030 cm^{-1}, as well as P−O−C bending vibrations (i.e., ν4 [PO_4] mode) at 770 and 539 cm^{-1}.[16,25] In addition, the N−H deformation vibration at 1590 cm^{-1} in CS is replaced by two new absorption peaks in CSP, that is, the symmetric and asymmetric deformation variations of $-NH_3^+$ at 1527 and 1630 cm^{-1}, respectively.[26] Moreover, the −OH bending vibration band at 1016 cm^{-1} vanishes and meanwhile the P−O stretching vibration peak appears at 1030 cm^{-1}. These phenomena indicate the phosphorylation of −OH groups and the successful conversion of CS into CSP. For the spectrum of CMC (Figure 2B), the peaks at 1405 and 1590 cm^{-1} result from the symmetric and asymmetric stretching vibration signals of −COO, respectively.[27] After the phosphorylation process, these two bands become weakened due to the suppression of strong P-related peaks in CMCP. In addition, the −OH bending vibration band at 1323 cm^{-1} disappears and

DOI: 10.1021/acssuschemeng.8b06416
ACS Sustainable Chem. Eng. 2019, 7, 5393−5403

a sharp peak corresponding to the free P−O stretching vibration appears at 1296 cm^{-1}. Moreover, the stretching vibration band of CH−O−CH_2 bond at 1023 cm^{-1} vanishes and two sharp peaks corresponding to the stretching vibrations of P−O−C bond appear at 1090 and 982 cm^{-1}.[18,25] These spectral changes suggest the phosphorylation of hydroxyl groups and the introduction of new phosphonate groups along the CMC chains.

For the FTIR data of CSP-CMCP (Figure 2C), the weak band at 1616 cm^{-1} results from the characteristic stretching vibration of C═O bond in the amide I groups, and that at 1527 cm^{-1} corresponds to the combined bending vibration of N−H bond and stretching vibration of C−N bond in the amide II groups.[28] These spectral features indicate that the cross-linking reaction occurs between the amino groups of CSP and the carboxyl sites of CMCP. The characteristic vibration band of the residual amino groups in CSP are possibly obscured by the absorption peaks of amide I and II groups. The bands at 1153, 1043, and 893 cm^{-1} result from the P−O stretching vibrations.[25] Herein, the CSP-CMCP composite is synthesized through the dehydration process between CSP and CMCP. According to the above FTIR analyses, the primary residual groups of CS and CMC after phosphorylation are the positively charged NH_3^+ and the negatively charged $-COO^-$, respectively. These two groups will form stable COO^-−NH_3^+ bonds with the aid of strong electrostatic attraction, the catalysis of MSP and the promotion of high temperature, leading to the generation of water-stable CSP-CMCP composite.[29] Figure 2D exhibits the relationship between the surface potential of CSP-CMCP and the pH value of solution. Clearly, the zeta potential gradually decreases with pH rising from 2.0 to 7.0, and then keeps almost constant at pH > 7.0. According to this variation trend, the zero point charge (i.e., pH_{zpc}) of CSP-CMCP is identified to be ∼3.80.

As shown in the TEM-derived elemental maps (Figure 3), phosphorus is abundant and uniformly distributed in the structure of CSP-CMCP. The plentiful phosphate groups are expected to greatly promote the adsorption capability of CSP-CMCP composite for U(VI). Based on the ICP-AES measurements after the dissolution experiments, the released P amounts from the CSP-CMCP composite are almost undetectable within pH 2.0−10.0. This result indicates that CSP-CMCP exhibits excellent physicochemical stability in both the acidic and alkaline solutions.

Macroscopic Adsorption Data. Figure 4A shows the adsorption data of U(VI) on CSP-CMCP with variable pH and ionic strength as the variables. Specifically, the adsorption efficiency sharply increases from ∼20% to ∼100% as the solution pH value rises from 2.0 to 5.5 and then keeps at the maximum level of ∼100% within pH 5.5−8.0. Afterward, the adsorption percentage exhibits a slightly decreasing trend at pH value above 8.0. This tendency can be explicated by considering the surface potentials of CSP-CMCP and the specific U(VI) species calculated from *Visual MINTEQ*, ver. 3.1 (Figure 4B).[30] The lower adsorption efficiency at pH < pH_{zpc} (i.e., 3.80 as shown in Figure 2D) arises from the electrostatic repulsion between the positively charged CSP-CMCP surfaces and the positive UO_2^{2+} species. As the solution pH exceeds the pH_{zpc} value, the surfaces of CSP-CMCP composite become negatively charged due to deprotonation. Hence, the positively charged $UO_2(OH)^+$, $(UO_2)_2(OH)_2^{2+}$, $(UO_2)_3(OH)_5^+$ and $(UO_2)_4(OH)_7^+$ species are easily adsorbed by the active sites on CSP-CMCP surfaces with the aid of strong electrostatic attraction. In contrast, the decrease of U(VI) adsorption percentage at pH > 8.0 results from the electrostatic repulsion between the negatively charged CSP-CMCP surfaces and U(VI) species (i.e., $UO_2(CO_3)_2^{2-}$ and $UO_2(CO_3)_3^{4-}$). As shown in Figure 4A, the adsorption trend of U(VI) on CSP-CMCP is not influenced by the variation of ionic strength over the entire pH range. In general, the background electrolyte ions can influence the adsorption procedures and binding modes of heavy metal ions onto the solid surfaces via the following paths: (1) alter the electric double layer thickness and interface potential of materials; (2) decrease the activity of heavy metal ions in solution; and (3) compete with the target metal ions for entering the cation exchange sites or binding on the adsorbent surfaces via electrostatic interaction (i.e., outer-sphere surface complexation).[6,31] Therefore, ion exchange and outer-sphere surface complexation are susceptible to the alteration of ionic strength in solution. In contrast, inner-sphere complexation is scarcely influenced by the background electrolyte ions. In view of the above points, the ionic strength-independent adsorption process of U(VI) on CSP-CMCP implies a removal mechanism of inner-sphere surface complexation.

Figure 4C shows the adsorption isotherm data of U(VI) on the CSP-CMCP composite at 293, 313, and 333 K. Apparently, the adsorption amount rises rapidly with increasing U(VI) equilibrium concentration (C_e) and ultimately reaches a plateau at a higher C_e value. This observation excludes the occurrence of homogeneous precipitation and/or heterogeneous coprecipitation, under which conditions the adsorption amount would exhibit an exponential growth trend. The adsorption isotherms are better simulated by the Langmuir model ($q_e = \frac{K_L q_{max} C_e}{1 + K_L C_e}$) than the Freundlich model ($q_e = K_F C_e^n$) for the adsorption isotherm data, suggesting a chemisorption mechanism of U(VI) on CSP-CMCP in a monolayer mode.[32,33] The maximum adsorption amounts (q_{max}) are calculated to be 977.54 mg/g at 293 K, 1043.40 mg/g at 313 K and 1174.69 mg/g at 333 K (Table 1). As listed in Table 2, the maximum adsorption capacity of CSP-CMCP toward U(VI) is higher than most of the adsorbents reported in the previous studies,[6,7,20,34−44] while a little inferior to the supramolecular organic frameworks-based solid phase extraction adsorbent (MA-TMA) and phosphonate-functionalized dendritic fibrous nanosilica (PA-DNFS).[45,46] This relatively high q_{max} value greatly enhances the application potentiality of the CSP-CMCP composite in the treatment of uranium-contaminated wastewaters.

Table 1. Parameters of Langmuir and Freundlich Model Fits for Equilibrium Adsorption Data of U(VI) on CSP-CMCP

	Langmuir			Freundlich		
temp (K)	K_L (L/mg)	q_{max} (mg/g)	R^2	K_F ($mg^{1-n}·L^n/g$)	n	R^2
293	0.12	977.54	0.99	258.75	0.281	0.97
313	0.13	1043.40	0.99	288.78	0.277	0.98
333	0.14	1174.69	0.98	344.69	0.266	0.97

Figure 4D illustrates the competitive adsorption behaviors of U(VI) and the coexisting metal ions on CSP-CMCP. At both the pH values of 3.0 and 5.0, the adsorption amounts (q_e, mg/g) of U(VI) are well above those of trivalent Cr(III), La(III), Eu(III), and Yb(III) as well as divalent Cu(II), Cd(II), Co(II),

DOI: 10.1021/acssuschemeng.8b06416
ACS Sustainable Chem. Eng. 2019, 7, 5393−5403

Table 2. Comparison of the Maximum Sorption Capacity of CSP-CMCP toward U(VI) with Other Adsorbents

adsorbents	exp conditions	q_{max} (mg/g)	refs
MWCNTs	pH = 5.0, T = 298 K	24.9	34
SZ-2	pH = 1.0, T = 298 K	58.18	6
Oxime-CMK-5	pH = 4.5, T = 298 K	65.18	20
GO nanosheets	pH = 5.5, T = 298 K	97.5	35
UiO-66-NH_2	pH = 5.5, T = 287 K	114.9	36
N-doped Fe/Fe_3C@C-800	pH = 6.0, T = 298 K	203	37
UiO-68-P(O)$(OEt)_2$	pH = 2.5, T = 298 K	217	38
Fe/N-C-700	pH = 6.0, T = 283 K	232.54	39
PA/TNTs	pH = 5.0, T = 293 K	276	40
GO-SH	pH = 5.0, T = 298 K	281.69	41
PAF-1-CH_2AO	pH = 6.0, T = 298 K	304	7
γ-Fe_2O_3/LDO	pH = 5.0, T = 303 K	526.32	42
MgO/carbon	pH = 4.0, T = 298 K	777.51	43
GO-CS-P	pH = 5.0, T = 293 K	779.44	44
CSP-CMCP	pH = 5.0, T = 293 K	977.54	this work
MA-TMA	pH = 5.0, T = 298 K	1028	45
PA-DFNS	pH = 8.0, T = 298 K	1106	46

and Sr(II). In detail, the corresponding S_U values are calculated to be ~100% and ~72% at pH 3.0 and 5.0, respectively. Obviously, CSP-CMCP exhibits an outstanding selectivity for separating U(VI) from the multicomponent solution. The higher adsorption priority of U(VI) than the coexisting metal ions can be interpreted by considering their intrinsic properties (e.g., oxidation state, charge-to-radius ratio (Z/r), first hydrolysis constant ($-\log \beta_1$)) and relative affinities to the functional groups on CSP-CMCP surfaces. Herein, U(VI) with a higher oxidation state and larger Z/r value (Table 3) are expected to exhibit a higher binding affinity on the surface sites of CSP-CMCP.[47−49] In addition, U(VI) is more easily to hydrolyze in solution due to its lower first hydrolysis constant ($-\log \beta_1$) value relative to the other competing cations.[50−52] Generally, the solid surfaces have a higher affinity toward the hydrolyzed species ($M(OH)_x^{n+}$) than the unhydrolyzed one (M^{n+}).[53] Therefore, U(VI) with a lower first hydrolysis constant is more easily retained by CSP-CMCP. Moreover, the preferential adsorption of U(VI) may be also due to its extremely high affinity and strong competitiveness for interacting with the surface phosphonate groups.[40,44]

Removal Mechanisms. Figure 5 displays the XRD patterns (A) and FTIR spectra (B) of CSP-CMCP before and after the adsorption of U(VI). Specifically, the absence of new diffraction peaks (Figure 5A) eliminates the precipitation of U(VI)-containing phases during the adsorption process. This conclusion is well consistent with that derived from the above adsorption isotherm analysis (Figure 4C). Several distinct features emerge in the FTIR spectrum of CSP-CMCP after U(VI) adsorption (Figure 5B). Specifically, the weak stretching vibration band of P−O at ~900 cm^{-1} is overlapped by a sharp and strong absorption peak originating from the stretching vibration of O−U−O bond.[44,54] In addition, the stretching vibration peak of P−O bond at 968 cm^{-1} shifts to a higher wavenumber and those at 1066 and 1022 cm^{-1} become muted. Moreover, the vibration peaks of amide and free $-NH_2$ groups exhibit some changes in their relative intensities. In specific, the peak intensity at 1527 cm^{-1} is slightly reduced and that at 1616 cm^{-1} is relatively enhanced. These phenomena suggest that both phosphonate and amino/$-NH_2$ sites contribute to the capture of U(VI).

Figure 6A displays the full scale XPS curves of CSP-CMCP composite before and after the retention of U(VI). Both spectra show the P 2p, C 1s, N 1s, and O 1s at ~134, ~285, ~400, and ~533 eV, respectively. In addition, an U 4f peak appears in the spectrum of U(VI)-adsorbed sample. As illustrated in Figure 6B and Table 4, the high-resolution U $4f_{5/2}$ and U $4f_{7/2}$ peaks are further subdivided into four components, that is, U(VI) $4f_{5/2}$ at 393.03 eV, U(IV) $4f_{5/2}$ at 391.33 eV, U(VI) $4f_{7/2}$ at 382.19 eV, and U(IV) $4f_{7/2}$ at 380.42 eV.[44,55] Based on the relative areas of their peaks, the proportions of U(VI) and U(IV) are fitted to be 73.3% and 26.7%, respectively. This result indicates that the adsorbed U(VI) is partly reduced to a lower U(IV) state by CSP-CMCP. The high-resolution C 1s spectra (Figure 6C) reveal three peaks, that is, 284.77 eV for $-CH_2$ and C−NH_2 bonds, 286.45 eV for C−O, C−O−P, C−OH, and C−N−C═O bonds, as well as 287.96 eV for O−C−O and N−C═O bonds.[25] No remarkable changes on the positions and relative areas of these peaks can be observed after U(VI) adsorption (Figure 6C and Table 4). In view of this, the related functional groups that participate in uranium immobilization can be deduced from the high-resolution spectra of P 2p, O 1s, and N 1s. Specifically, the P 2p spectrum of uranium-containing sample shows a blue shift relative to that of the pristine CSP-CMCP composite (Figure 6D and Table 4). This difference indicates that the phosphate groups play a vital role in U(VI) removal. The complicated O-containing components can provide additional information for identifying the immobilization mechanisms. The O 1s peaks of CSP-CMCP composite before and after U(VI) uptake are split into the similar four peaks. Specifically, the O 1s peak of pure CSP-CMCP composite are composed of P−O at 531.00 eV, N−C═O and O−C═O at 532.03 eV, −OH at 532.46 eV as well as O−C−O and C−O−P at 533.11 eV (Figure 6E and Table 4).[25,44] Both the positions and the relative proportions of these O-donor functional groups exhibit apparent changes after uranium adsorption (Figure 6E and Table 4).

Some obvious differences can be also observed for the high-resolution N 1s spectra before and after the adsorption of U(VI). For the N 1s spectrum of the pristine CSP-CMCP composite (Figure 6F), the peak at 399.58 eV corresponds to N−C═O and $-NH_2$ groups, while that at 401.49 eV is assigned to the protonated amino group (i.e., NH_3^+; Table 4) due to the extremely acidic condition in the phosphorylation

Table 3. Physicochemical Properties of U(VI) and the Coexisting Metal Ions

metal properties	Sr(II)	Cd(II)	Co(II)	Cu(II)	Cr(III)	La(III)	Eu(III)	Y(III)	U(VI)
oxidation state	+2	+2	+2	+2	+3	+3	+3	+3	+6
ionic radius (Å)	1.13	0.97	0.72	0.70	0.69	1.03	0.98	0.86	0.73
charge to radius ratio (Z/r)	1.78	2.06	2.78	2.86	4.35	2.91	3.06	3.49	8.22
first hydrolysis constant ($-\log \beta 1$)	24.96	10.08	9.60	7.53	6.84	8.81	7.76	7.24	5.29

DOI: 10.1021/acssuschemeng.8b06416
ACS Sustainable Chem. Eng. 2019, 7, 5393−5403

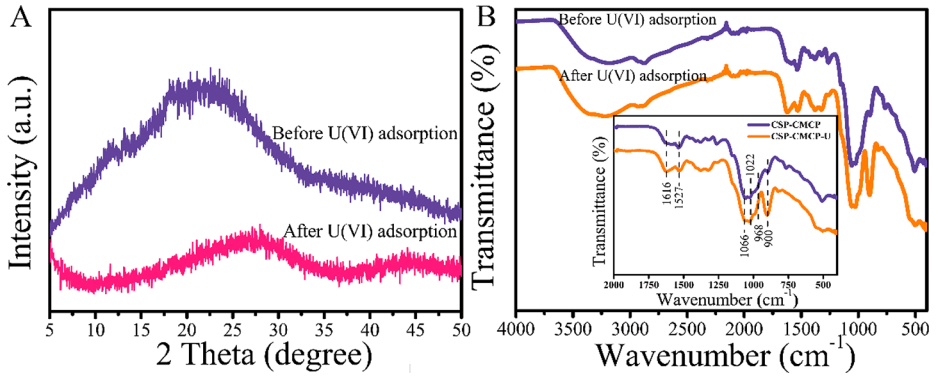

Figure 5. XRD patterns (A) and FTIR spectra (B) of CSP-CMCP before and after U(VI) adsorption. T = 293 K, pH = 5.0, m/V = 0.05 g/L, $C_{U(VI)initial}$ = 5.0 × 10^{-5} mol/L, I = 0.01 mol/L $NaNO_3$.

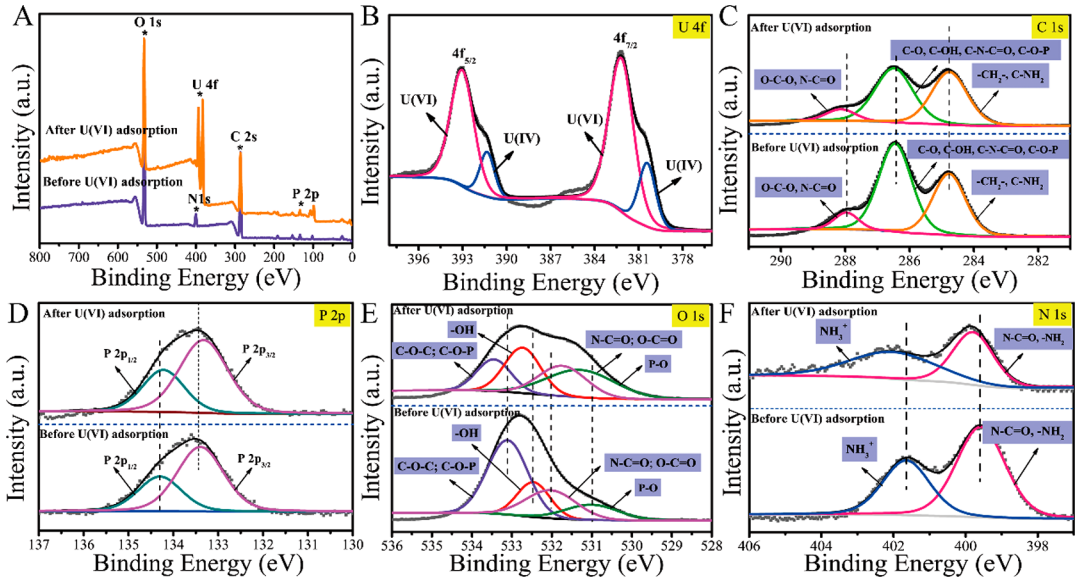

Figure 6. (A) XPS survey scans of CSP-CMCP composite before and after U(VI) adsorption (A); High-resolution U 4f XPS spectrum of U(VI)-loaded CSP-CMCP (B); High-resolution C 1s (C), P 2p (D), O 1s (E), and N 1s (F) spectra before and after U(VI) adsorption. T = 293 K, pH = 5.0, m/V = 0.05 g/L, $C_{U(VI)initial}$ = 5.0 × 10^{-5} mol/L, I = 0.01 mol/L $NaNO_3$.

Table 4. Binding Energies (eV) of C 1s, O 1s, N 1s, P 2p, and U 4f before and after U(VI) Adsorption onto CSP-CMCP

valence states		samples	before U(VI) adsorption	after U(VI) adsorption
C 1s		$-CH_2$, C-NH_2	284.77	284.76
		C−O, C−OH, C−O−P, C−N−C=O	286.45	286.49
		O−C−O, N−C=O	287.96	288.14
O 1s		P−O	531.00	531.29
		N−C=O	532.03	531.74
		C−OH	532.46	532.73
		O−C−O, C−O−P	533.11	533.45
N 1s		N−C=O, $-NH_2$	399.58	399.79
		NH_3^+	401.49	402.02
P 2p	P $2p_{3/2}$		133.40	133.33
	P $2p_{1/2}$		134.30	134.22
U 4f	U $4f_{7/2}$	U(IV)		380.42
		U(VI)		382.19
	U $4f_{5/2}$	U(IV)		391.33
		U(VI)		393.03

process.[56,57] Both the positions and intensities of these two peaks exhibit obvious changes after U(VI) adsorption. Note that some of the protonated NH_3^+ sites on CSP-CMCP surfaces may be possibly converted into the free $-NH_2$ form due to the deprotonation reaction during the pH adjustment process, that is, S-NH_3^+ ↔ S-NH_2 + H^+ (herein, S represents the surfaces of CSP-CMCP composite). Under such circumstances, a charge transfer from the active amino sites to the U(VI) species would possibly happen and therefore results in the conversion of U(VI) into U(IV).[56] In a series of previous studies, the reduction of Cu(II), Hg(II), Cr(VI) and Mo(VI) and U(VI) by natural and cross-linked CS was ascribed to the following two aspects: (1) the terminal D-glucosamine in the CS structure (i.e., the free NH_2 sites) acted as the predominant reducing agent; and (2) the reductive activity of CS toward metal ions could be reinforced by exposing to the visual light.[58,59] Herein, the similar reduction phenomena may also occur during the retention process of U(VI) by CS-CMCP. In light of the above discussions, one can make a conclusion that the phosphonate and amino sites on the surfaces of CS-CMCP composite contribution to the complexation and reduction of U(VI).

DOI: 10.1021/acssuschemeng.8b06416
ACS Sustainable Chem. Eng. 2019, 7, 5393−5403

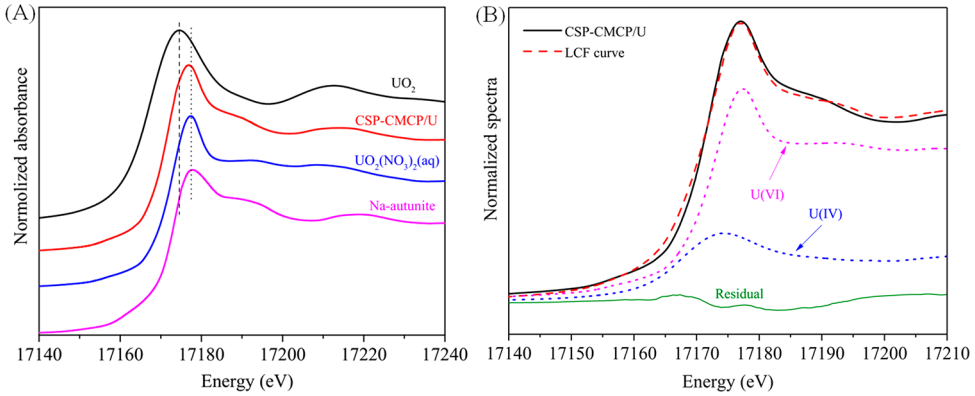

Figure 7. (A) XANES spectra of U-containing reference and adsorption samples; (B) Linear combination fitting (LCF) on the XANES spectrum of CSP-CMCP/U sample.

The XAS analysis is further adopted to verify the valence state and local structure of uranium on CSP-CMCP composite. Figure 7A displays the L_{III}-edge XANES spectra of U-related standard components and adsorption sample. The X-ray absorption peaks of U(IV) (i.e., UO_2) and U(VI) (i.e., $UO_2(NO_3)_2$(aq) and Na-autunite) components are located at 17174.5 (see the dash line) and 17177.6 eV (see the dot line), respectively. Herein, the X-ray adsorption peak CSP-CMCP/U (i.e., 17177.2 eV) is located between those of U(IV) and U(VI) but more close to that of U(VI). It seems that the immobilized U(VI) on CSP-CMCP surfaces is partially reduced to U(IV). Based on the linear combination fitting embedded in the Athena software, the relative proportions of U(VI) and U(IV) are calculated to be 77.6% and 22.4%, respectively (Figure 7B). The relative ratios are well consistent with those derived from the above XPS analysis, that is, 73.3% for U(VI) and 26.7% for U(IV) (Figure 6B).

The $k^3\chi(k)$ EXAFS spectrum of CSP-CMCP/U sample apparently differs from those of $UO_2(NO_3)_2$(aq) and Na-autunite within the k range of 6.5−11.0 (marked by a rectangle; Figure 8A). In this case, one can eliminate the occurrence of cation exchange, outer-sphere complexation or Na-autunite precipitation. For all the U-containing samples, the corresponding RSFs (Figure 8B, no correction for phase shift) show two high-intensity peaks at 1.37 Å (originating from the backscattering signals of axial O atoms) and 1.89 Å (originating from the backscattering signals of equatorial O and N atoms). In addition, more peaks appear in the RSFs of CSP-CMCP/U (centered at 2.40 Å, 2.66 and 3.10 Å) and Na-autunite (centered at 3.01 and 4.97 Å). Herein, the characteristic peak at 4.97 Å in the RSF of Na-autunite results from the backscattering of the U−U shell. The absence of this peak in the RSF of CSP-CMCP/U further rules out the precipitation of Na-autunite during the adsorption process. The structural parameters derived from the least-squares fitting of RSFs are listed in Table 5. The central U atom in the CSP-CMCP/U sample is surrounded by 4.5 O/N atoms at $R_{U\text{-}Oeq}$/N of 2.36 Å, 1.1 C atoms at R_{U-C} of 2.91 Å, 1.8 P atoms at R_{U-P1} of 3.10 Å (i.e., bidentate U(IV)-phosphonate complexation) and 1.2 P atoms at R_{U-P2} of 3.65 Å (i.e., monodentate U(VI)-phosphonate complexation). This fitting result suggests the collaborative involvement of amino and phosphonate groups on CSP-CMCP surfaces for immobilizing U(VI).[60] This conclusion is well consistent with that proposed from the above-mentioned FTIR and XPS analyses.

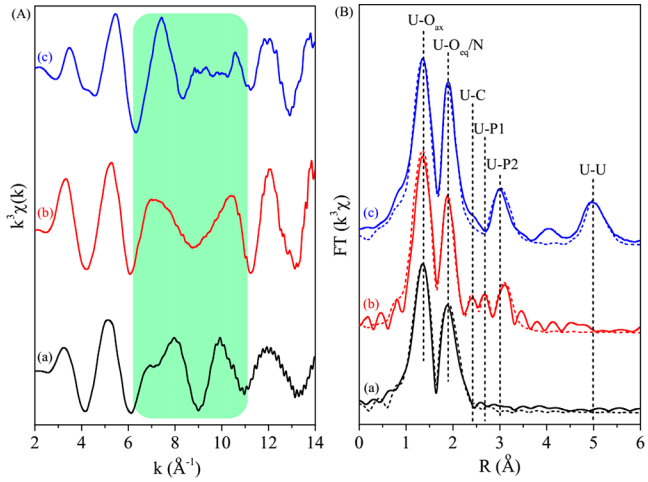

Figure 8. k^3-weighted EXAFS spectra and the corresponding RSFs (uncorrected for phase shift) of U-containing reference (a: $UO_2(NO_3)_2$(aq); c: Na-autunite) and adsorption (b: CSP-CMCP/U) samples. (A) Solid lines represent the experimental k^3-weighted EXAFS spectra; (B) Solid lines represent the experimental RSF magnitudes and dash lines represent the spectral fits. T = 293 K, pH = 5.0, m/V = 0.05 g/L, $C_{U(VI)initial}$ = 5.0 × 10^{-5} mol/L, I = 0.01 mol/L $NaNO_3$.

Table 5. Structural Parameters of U-Containing Samples Derived from EXAFS Analyses[a]

sample	shell	R (Å)	CN	σ^2 (Å^2)
$UO_2(NO_3)_2$(aq)	U−O_{ax}	1.79(2)	2.0[b]	0.0028(2)
	U−O_{eq}	2.35(3)	3.8(3)	0.0041(3)
CSP-CMCP/U	U−O_{ax}	1.78(2)	2.0[b]	0.0033(2)
	U−O_{eq}/N	2.36(3)	4.5(2)	0.0045(3)
	U−C	2.91(3)	1.1(3)	0.0050(4)
	U−P1	3.10(4)	1.8(3)	0.0064(4)
	U−P2	3.65(3)	1.2(4)	0.0068(5)
Na-autunite	U−O_{ax}	1.78(1)	2.0[b]	0.0034(2)
	U−O_{eq}	2.35(2)	3.9(2)	0.0042(4)
	U−P	3.59(4)	4.0(3)	0.0058(3)
	U−U	5.21(3)	3.8(3)	0.0074(4)

[a]R, bond distance; CN, coordination number; σ^2, Debye−Waller factor. [b]Fixed or constrained during spectral fitting. The estimated standard deviations are listed in parentheses, representing the error in the last digit.

DOI: 10.1021/acssuschemeng.8b06416
ACS Sustainable Chem. Eng. 2019, 7, 5393−5403

CONCLUSIONS

This work reports the rational design and synthesis of a novel CSP-CMCP composite for the potential removal of radioactive U(VI) from the polluted aquatic systems. The usage of nontoxic CS and CMC with abundant source as the precursors guarantees the environmental friendliness and low cost of the CSP-CMCP composite. In addition, the easy synthesis of CSP-CMCP via strong cross-linking between amino and carboxyl sites empowers its excellent stability in a broad pH range. As expected, the prepared CSP-CMCP exhibits good removal performance and excellent adsorption selectivity for U(VI). The inner-sphere surface complexation is identified to be the predominant removal mechanism. In addition, the reduction of a small proportion of U(VI) to U(IV) also occurs in the retention process. Considering its multiple advantages as mentioned above, the CSP-CMCP composite can be potentially applied in the purification of uranium-contaminated groundwater.

AUTHOR INFORMATION

Corresponding Authors

*E-mail: shitongyang-dmn@outlook.com.
*E-mail: shuaowang@suda.edu.cn. Tel.: +81-3-5841-4506. Fax: +81-3-5841-4506.

ORCID

Shitong Yang: 0000-0002-3083-5485
Haibo Qin: 0000-0002-7404-3703
Xiangke Wang: 0000-0002-3352-1617
Shuao Wang: 0000-0002-1526-1102

Author Contributions

#Y.C. and L.C. made an equal contribution to this paper.

Notes

The authors declare no competing financial interest.

ACKNOWLEDGMENTS

We acknowledged the research funding supports (Grant Nos. 21790370, U1732132, 41773004) of National Natural Science Foundation of China and the Priority Academic Program Development (PAPD) of Jiangsu Higher Education Institutions.

REFERENCES

(1) Asic, A.; Kurtovic-Kozaric, A.; Besic, L.; Mehinovic, L.; Hasic, A.; Kozaric, M.; Hukic, M.; Marjanovic, D. Chemical toxicity and radioactivity of depleted uranium: The evidence from in vivo and in vitro studies. *Environ. Res.* **2017**, *156*, 665−673.

(2) Yang, S. T.; Zong, P. F.; Hu, J.; Sheng, G. D.; Wang, Q.; Wang, X. K. Fabrication of β-cyclodextrin conjugated magnetic HNT/iron oxide composite for high-efficient decontamination of U(VI). *Chem. Eng. J.* **2013**, *214*, 376−385.

(3) Mikhaylov, V. I.; Krivoshapkina, E. F.; Trigub, A. L.; Stalugin, V. V.; Krivoshapkin, P. V. Detection and Adsorption of Cr(VI) ions by Mesoporous Fe-Alumina Films. *ACS Sustainable Chem. Eng.* **2018**, *6*, 9283−9292.

(4) Cheng, W. C.; Ding, C. C.; Nie, X. Q.; Duan, T.; Ding, R. R. Fabrication of 3D Macroscopic Graphene Oxide Composites Supported by Montmorillonite for Efficient U(VI) Wastewater Purification. *ACS Sustainable Chem. Eng.* **2017**, *5*, 5503−5511.

(5) Sun, Y. B.; Yang, S. B.; Chen, Y.; Ding, C. C.; Cheng, W. C.; Wang, X. K. Adsorption and Desorption of U(VI) on Functionalized Graphene Oxides: A Combined Experimental and Theoretical Study. *Environ. Sci. Technol.* **2015**, *49*, 4255−4262.

(6) Zheng, T.; Yang, Z. X.; Gui, D. X.; Liu, Z. Y.; Wang, X. X.; Dai, X.; Liu, S. T.; Zhang, L. J.; Gao, Y.; Chen, L. H.; Sheng, D. P.; Wang, Y. L.; Diwu, J.; Wang, J. Q.; Zhou, R. H.; Chai, Z. F.; Albrecht-Schmitt, T. E.; Wang, S. A. Overcoming the crystallization and designability issues in the ultrastable zirconium phosphonate framework system. *Nat. Commun.* **2017**, *8*, 15369.

(7) Li, B. Y.; Sun, Q.; Zhang, Y. M.; Abney, C. W.; Aguila, B.; Lin, W. B.; Ma, S. Q. Functionalized Porous Aromatic Framework for Efficient Uranium Adsorption from Aqueous Solutions. *ACS Appl. Mater. Interfaces* **2017**, *9*, 12511−12517.

(8) Duan, S. X.; Wang, Y. N.; Liu, X.; Shao, D. D.; Hayat, T.; Alsaedi, A.; Li, J. X. Removal of U(VI) from Aqueous Solution by Amino Functionalized Flake Graphite Prepared by Plasma Treatment. *ACS Sustainable Chem. Eng.* **2017**, *5*, 4073−4085.

(9) Muzzarelli, R. A. A. Potential of chitin/chitosan-bearing materials for uranium recovery: An interdisciplinary review. *Carbohydr. Polym.* **2011**, *84*, 54−63.

(10) Pu, S. Y.; Hou, Y. G.; Yan, C.; Ma, H.; Huang, H. Y.; Shi, Q. Q.; Mandal, S.; Diao, Z. H.; Chu, W. In Situ Co-Precipitation Formed Highly Water-Dispersible Magnetic Chitosan Nanopowder for Removal of Heavy Metals and Its Adsorption Mechanism. *ACS Sustainable Chem. Eng.* **2018**, *6*, 16754−16765.

(11) Rinaudo, M. Chitin and chitosan: Properties and applications. *Prog. Polym. Sci.* **2006**, *31*, 603−632.

(12) Biswal, D. R.; Singh, R. P. Characterisation of carboxymethyl cellulose and polyacrylamide graft copolymer. *Carbohydr. Polym.* **2004**, *57*, 379−387.

(13) Ho, T. L. The Hard Soft Acids Bases (HSAB) Principle and Organic Chemistry. *Chem. Rev.* **1975**, *75*, 1−20.

(14) Sarsfield, M. J.; Helliwell, M. Extending the Chemistry of the Uranyl Ion: Lewis Acid Coordination to a U = O Oxygen. *J. Am. Chem. Soc.* **2004**, *126*, 1036−1037.

(15) Galand, N.; Wipff, G. Uranyl extraction by α-Diketonate ligands to SC-CO(2): Theoretical studies on the effect of ligand fluorination and on the synergistic effect of TBP. *J. Phys. Chem. B* **2005**, *109*, 277−287.

(16) Li, Q. L.; Chen, Z. Q.; Darvell, B. W.; Liu, K. H.; Jiang, B.; Zen, Q.; Peng, Q.; Ou, G. M. Chitosan-Phosphorylated Chitosan Polyelectrolyte Complex Hydrogel as an Osteoblast Carrier. *J. Biomed. Mater. Res., Part B* **2007**, *82*, 481−486.

(17) Jayakumar, R.; Selvamurugan, N.; Nair, S. V.; Tokura, S.; Tamura, H. Preparative methods of phosphorylated chitin and chitosan-An overview. *Int. J. Biol. Macromol.* **2008**, *43*, 221−225.

(18) Leone, G.; Torricelli, P.; Giardino, R.; Barbucci, R. New phosphorylated derivatives of carboxymethylcellulose with osteogenic activity. *Polym. Adv. Technol.* **2008**, *19*, 824−830.

(19) Zhao, D.; Zhao, L.; Zhu, C. S.; Tian, Z. B.; Shen, X. Y. Synthesis and properties of water-insoluble β-cyclodextrin polymer crosslinked by citric acid with PEG-400 as modifier. *Carbohydr. Polym.* **2009**, *78*, 125−130.

(20) Tian, G.; Geng, J. X.; Jin, Y. D.; Wang, C. L.; Li, S. Q.; Chen, Z.; Wang, H.; Zhao, Y. S.; Li, S. J. Sorption of uranium(VI) using oxime-grafted ordered mesoporous carbon CMK-5. *J. Hazard. Mater.* **2011**, *190*, 442−450.

(21) Ravel, B.; Newville, M. ATHENA, ARTEMIS, HEPHAESTUS: data analysis for X-ray absorption spectroscopy using IFEFFIT. *J. Synchrotron Radiat.* **2005**, *12*, 537−541.

(22) Templeton, D. H.; Zalkin, A.; Ruben, H.; Templeton, L. K. Redetermination and absolute configuration of sodium uranyl(VI) triacetate. *Acta Crystallogr., Sect. C: Cryst. Struct. Commun.* **1985**, *C41*, 1439−1441.

(23) Dusausoy, Y.; Ghermani, N. E.; Podor, R.; Cuney, M. Low-temperature ordered phase of $CaU(PO_4)_2$: synthesis and crystal structure. *Eur. J. Mineral.* **1996**, *8*, 667−674.

(24) Morosin, B. Hydrogen Uranyl Phosphate Tetrahydrate, a Hydrogen Ion Solid Electrolyte. *Acta Crystallogr., Sect. B: Struct. Crystallogr. Cryst. Chem.* **1978**, *B34*, 3732−3734.

DOI: 10.1021/acssuschemeng.8b06416
ACS Sustainable Chem. Eng. 2019, 7, 5393−5403

(25) Amaral, I. F.; Granja, P. L.; Barbosa, M. A. Chemical modification of chitosan by phosphorylation: an XPS, FT-IR and SEM study. *J. Biomater. Sci., Polym. Ed.* **2005**, *16*, 1575−1593.
(26) Hu, S.; Song, L.; Pan, H. F.; Hu, Y.; Gong, X. L. Thermal properties and combustion behaviors of flame retarded epoxy acrylate with a chitosan based flame retardant containing phosphorus and acrylate structure. *J. Anal. Appl. Pyrolysis* **2012**, *97*, 109−115.
(27) Lan, W. T.; He, L.; Liu, Y. W. Preparation and Properties of Sodium Carboxymethyl Cellulose/Sodium Alginate/Chitosan Composite Film. *Coatings* **2018**, *8*, 291.
(28) Lawrie, G.; Keen, I.; Drew, B.; Chandler-Temple, A.; Rintoul, L.; Fredericks, P.; Grøndahl, L. Interactions between Alginate and Chitosan Biopolymers Characterized Using FTIR and XPS. *Biomacromolecules* **2007**, *8*, 2533−2541.
(29) Yoncheva, K.; Popova, M.; Szegedi, A.; Mihaly, J.; Tzankov, B.; Lambov, N.; Konstantinov, S.; Tzankova, V.; Pessina, F.; Valoti, M. Functionalized mesoporous silica nanoparticles for oral delivery of budesonide. *J. Solid State Chem.* **2014**, *211*, 154−161.
(30) Gustafsson, J. P. Visual MINTEQ, ver. 3.1, Department of Land and Water Resources Engineering, KTH, SE-100 44, Stockholm, Sweden; available at the website of https://vminteq.lwr.kth.se/download/.
(31) Hayes, K. F.; Papelis, C.; Leckie, J. O. Modeling Ionic Strength Effects on Anion Adsorption at Hydrous Oxide/Solution Interfaces. *J. Colloid Interface Sci.* **1988**, *125*, 717−726.
(32) Abraham, P. M.; Barnikol, S.; Baumann, T.; Kuehn, M.; Ivleva, N. P.; Schaumann, G. E. Sorption of Silver Nanoparticles to Environmental and Model Surfaces. *Environ. Sci. Technol.* **2013**, *47*, 5083−5091.
(33) Wu, J.; Zhu, H. S.; Liu, G.; Tan, L. Q.; Hu, X. Y.; Chen, C. L.; Alharbi, N. S.; Hayat, T.; Tan, X. L. abrication of Core-Shell CMNP@PmPD Nanocomposite for Efficient As(V) Adsorption and Reduction. *ACS Sustainable Chem. Eng.* **2017**, *5*, 4399−4407.
(34) Fasfous, I. I.; Dawoud, J. N. Uranium (VI) sorption by multiwalled carbon nanotubes from aqueous solution. *Appl. Surf. Sci.* **2012**, *259*, 433−440.
(35) Zhao, G. X.; Wen, T.; Yang, X.; Yang, S. B.; Liao, J. L.; Hu, J.; Shao, D. D.; Wang, X. K. Preconcentration of U(VI) ions on few-layered graphene oxide nanosheets from aqueous solutions. *Dalton Trans* **2012**, *41*, 6182−6188.
(36) Luo, B. C.; Yuan, L. Y.; Chai, Z. F.; Shi, W. Q.; Tang, Q. U(VI) capture from aqueous solution by highly porous and stable MOFs: UiO-66 and its amine derivative. *J. Radioanal. Nucl. Chem.* **2016**, *307*, 269−276.
(37) Wen, T.; Wang, X. X.; Wang, J.; Chen, Z. S.; Li, J. X.; Hu, J.; Hayat, T.; Alsaedi, A.; Grambow, B.; Wang, X. K. A strategically designed porous magnetic N-doped Fe/Fe_3C@C matrix and its highly efficient uranium(VI) remediation. *Inorg. Chem. Front.* **2016**, *3*, 1227−1235.
(38) Carboni, M.; Abney, C. W.; Liu, S. B.; Lin, W. B. Highly porous and stable metal-organic frameworks for uranium extraction. *Chem. Sci.* **2013**, *4*, 2396−2402.
(39) Zhu, K.; Chen, C. L.; Xu, M. W. C.; Chen, K.; Tan, X. L.; Wakeel, M.; Alharbi, N. S. In situ carbothermal reduction synthesis of Fe nanocrystals embedded into N-doped carbon nanospheres for highly efficient U(VI) adsorption and reduction. *Chem. Eng. J.* **2018**, *331*, 395−405.
(40) Yuan, F.; Wu, C. F.; Cai, Y. W.; Zhang, L. J.; Wang, J. Q.; Chen, L. H.; Wang, X. K.; Yang, S. T.; Wang, S. A. Synthesis of phytic acid-decorated titanate nanotubes for high efficient and high selective removal of U(VI). *Chem. Eng. J.* **2017**, *322*, 353−365.
(41) Zhao, D. L.; Gao, X.; Chen, S. H.; Xie, F. Z.; Feng, S. J.; Alsaedi, A.; Hayat, T.; Chen, C. L. Interaction between U(VI) with sulfhydryl groups functionalized graphene oxides investigated by batch and spectroscopic techniques. *J. Colloid Interface Sci.* **2018**, *524*, 129−138.
(42) Zhu, K.; Chen, C. L.; Wang, H. Y.; Xie, Y.; Wakeel, M.; Wahid, A.; Zhang, X. D. Gamma-ferric oxide nanoparticles decoration onto porous layered double oxide belts for efficient removal of uranyl. *J. Colloid Interface Sci.* **2019**, *535*, 265−275.
(43) Lv, Z. M.; Wang, H. Y.; Chen, C. L.; Yang, S. M.; Chen, L.; Alsaedi, A.; Hayat, T. Enhanced removal of uranium(VI) from aqueous solution by a novel Mg-MOF-74-derived porous MgO/carbon adsorbent. *J. Colloid Interface Sci.* **2019**, *537*, A1−A10.
(44) Cai, Y. W.; Wu, C. F.; Liu, Z. Y.; Zhang, L. J.; Chen, L. H.; Wang, J. Q.; Wang, X. K.; Yang, S. T.; Wang, S. A. Fabrication of a phosphorylated graphene oxide-chitosan composite for highly effective and selective capture of U(VI). *Environ. Sci.: Nano* **2017**, *4*, 1876−1886.
(45) Li, B.; Bai, C. Y.; Zhang, S.; Zhao, X. S.; Li, Y.; Wang, L.; Ding, K.; Shu, X.; Li, S. J.; Ma, L. J. An adaptive supramolecular organic framework for highly efficient separation of uranium via an in situ induced fit mechanism. *J. Mater. Chem. A* **2015**, *3*, 23788.
(46) Yang, P. P.; Liu, Q.; Liu, J. Y.; Chen, R. R.; Li, R. M.; Bai, X. F.; Wang, J. Highly efficient immobilization of uranium(VI) from aqueous solution by phosphonate-functionalized dendritic fibrous nanosilica (DFNS). *J. Hazard. Mater.* **2019**, *363*, 248−257.
(47) Lv, L.; Tsoi, G.; Zhao, X. S. Uptake Equilibria and Mechanisms of Heavy Metal Ions on Microporous Titanosilicate ETS-10. *Ind. Eng. Chem. Res.* **2004**, *43*, 7900−7906.
(48) Lansman, J. B. Blockade of Current through Single Calcium Channels by Trivalent Lanthanide Cations. *J. Gen. Physiol.* **1990**, *95*, 679−696.
(49) Arnold, P. L.; Love, J. B.; Patel, D. Pentavalent uranyl complexes. *Coord. Chem. Rev.* **2009**, *253*, 1973−1978.
(50) Yavuz, O.; Altunkaynak, Y.; Güzel, F. Removal of copper, nickel, cobalt andmanganese from aqueous solution by kaolinite. *Water Res.* **2003**, *37*, 948−952.
(51) Bentouhami, E.; Bouet, G. M.; Meullemeestre, J.; Vierling, F.; Khan, M. A. Physicochemical study of the hydrolysis of Rare-Earth elements (III) and thorium (IV). *C. R. Chim.* **2004**, *7*, 537−545.
(52) Krestou, A.; Xenidis, A.; Panias, D. Mechanism of aqueous uranium(VI) uptake by hydroxyapatite. *Miner. Eng.* **2004**, *17*, 373−381.
(53) Saha, U. K.; Taniguchi, S.; Sakurai, K. Simultaneous Adsorption of Cadmium, Zinc, and Lead on Hydroxyaluminum- and Hydroxyaluminosilicate-Montmorillonite Complexes. *Soil Sci. Soc. Am. J.* **2002**, *66*, 117−128.
(54) Song, Y. F.; Hu, Q. H.; Li, T. M.; Sun, Y. K.; Chen, X. X.; Fan, J. Fabrication and characterization of phosphorylated chitosan nanofiltration membranes with tunable surface charges and improved selectivities. *Chem. Eng. J.* **2018**, *352*, 163−172.
(55) Wang, L.; Song, H.; Yuan, L. Y.; Li, Z. J.; Zhang, Y. J.; Gibson, J. K.; Zheng, L. R.; Chai, Z. F.; Shi, W. Q. Efficient U(VI) Reduction and Sequestration by Ti_2CT_x MXene. *Environ. Sci. Technol.* **2018**, *52*, 10748−10756.
(56) Ang, A. K. S.; Kang, E. T.; Neoh, K. G.; Tan, K. L.; Cui, C. Q.; Lim, T. B. Low-temperature graft copolymerization of 1-vinyl imidazole on polyimide films with simultaneous lamination to copper foils-effect of crosslinking agents. *Polymer* **2000**, *41*, 489−498.
(57) Zhang, H. L.; Li, P.; Wang, M.; Cui, W. W.; Zhang, Y.; Zhang, Y.; Zheng, S. L.; Zhang, Y. Sustainable Disposal of Cr(VI): Adsorption-Reduction Strategy for Treating Textile Wastewaters with Amino-Functionalized Boehmite Hazardous Solid Wastes. *ACS Sustainable Chem. Eng.* **2018**, *6*, 6811−6819.
(58) Huang, X. X.; Liu, Y. G.; Liu, S. B.; Tan, X. F.; Ding, Y.; Zeng, G. M.; Zhou, Y. Y.; Zhang, M. M.; Wang, S. F.; Zheng, B. H. Effective removal of Cr(VI) using β-cyclodextrin-chitosan modified biochars with adsorption/reduction bifuctional roles. *RSC Adv.* **2016**, *6*, 94−104.
(59) Dang, N. V. K.; Kowandy, C.; Dupont, L.; Coqueret, X. Evidence of chitosan-mediated reduction of Au(III) to Au(0) nanoparticles under electron beam by using $OH^{\bullet}$ and e^{-}_{aq} scavengers. *Chem. Commun.* **2015**, *51*, 4017−4020.
(60) Kelly, S. D.; Kemner, K. M.; Fein, J. B.; Fowle, D. A.; Boyanov, M. I.; Bunker, B. A.; Yee, N. X-ray absorption fine structure

DOI: 10.1021/acssuschemeng.8b06416
ACS Sustainable Chem. Eng. 2019, 7, 5393−5403

determination of pH-dependent U-bacterial cell wall interactions. *Geochim. Cosmochim. Acta* **2002**, *66*, 3855−3871.

DOI: 10.1021/acssuschemeng.8b06416
ACS Sustainable Chem. Eng. 2019, 7, 5393−5403